npj | climate and atmospheric science

Article

Published in partnership with CECCR at King Abdulaziz University

https://doi.org/10.1038/s41612-024-00639-9

Unexpected HCHO transnational transport: influence on the temporal and spatial distribution of HCHO in Tibet from 2013 to 2021 based on satellite

Yizhou Xu[1], Wenjing Su[2] ✉, Qihou Hu[3], Chengxin Zhang[1], Zeeshan Javed[4], Yuan Tian[5], Hongri Hou[3] & Cheng Liu[1,3,6,7] ✉

Formaldehyde (HCHO) is a serious hazardous air pollutant and crucial precursor of $PM_{2.5}$ and ozone compound pollution. There has been a dearth of HCHO research in Tibet where pressing need to protect the unique ecosystem. Therefore, this study aims to investigate the spatial-temporal distribution of HCHO from 2013 to 2021 and identify its influencing factors using satellite observations. Our findings reveal a noteworthy annual growth rate of 2.25% yr^{-1} in HCHO vertical column density (VCD) in Tibet. This rate is comparable to that in India and even surpasses levels observed in many other regions worldwide, including eastern China. Furthermore, unlike other areas, the eastern region of Tibet exhibits no discernible seasonal pattern in HCHO VCD. The anomalous variation in HCHO concentrations in Tibet can primarily be attributed to long-distance transnational transport originating from incomplete combustion in India Assam. Our research underscores the urgent need for enhanced atmospheric environmental management in Tibet.

Formaldehyde (HCHO) plays a vital role in atmospheric chemical processes. As one of the most important reactive oxygenated volatile organic compounds (VOCs) and a significant source of hydroxyl radicals ($HO_x = OH + HO_2$)[1], HCHO affects atmospheric oxidation capacity[2]. The HO_x created by HCHO can further react with carbon monoxide (CO), nitrogen oxides (NO_x), and VOCs, producing oxygen (O_3), second organic aerosol, and peroxyacetyl nitrate (PAN), resulting in severe compound atmospheric pollution[3–5]. In addition, HCHO has been listed in 187 hazardous air pollutants by the US Environment Protection Agency and is classified as carcinogenic to humans by the World Health Organization[6]. A previous study showed that short-term exposure to low-level ambient HCHO increases mortality risks in non-accidental, circulatory, and respiratory diseases[7].

Atmospheric HCHO originates from various sources, such as fossil fuel combustion, vehicle exhaust, and photochemical reactions. Depending on the difference in the formation pathway, these sources can be categorized into primary and secondary sources, and the secondary formation of VOC oxidation is an important source of HCHO[8]. In line with efforts to mitigate pollution, the National Fourteenth Five-Year Plan of China has been implemented, which includes measures to reduce various pollutants, including VOCs. Given that HCHO serves as a key indicator of VOC oxidation capacity, it is essential to investigate China's HCHO emission and distribution. Long-term and wide-area HCHO monitoring is vital for improving the atmospheric environment and public health[9].

Various off-line sampling and online analysis techniques for atmospheric HCHO monitoring have been developed. Notably, several widely employed methods include 2,4-dinitrophenylhydrazine derivatization combined with high-performance liquid chromatography (DNPH-HPLC)[10], proton transfer reaction mass spectrometry (PTR-MS)[11], tunable

[1]Department of Precision Machinery and Precision Instrumentation, University of Science and Technology of China, Hefei 230026, China. [2]Department of Environmental Science and Engineering, University of Science and Technology of China, Hefei 230026, China. [3]Key Laboratory of Environmental Optics and Technology, Anhui Institute of Optics and Fine Mechanics, Chinese Academy of Sciences, Hefei 230031, China. [4]Key Laboratory for Semi-Arid Climate Change of the Ministry of Education, College of Atmospheric Sciences, Lanzhou University, Lanzhou 730000, China. [5]Institutes of Physical Science and Information Technology, Anhui University, Hefei 230601, China. [6]Center for Excellence in Regional Atmospheric Environment, Institute of Urban Environment, Chinese Academy of Sciences, Xiamen 361021, China. [7]Key Laboratory of Precision Scientific Instrumentation of Anhui Higher Education Institutes, University of Science and Technology of China, Hefei 230026, China. ✉e-mail: swj1993@mail.ustc.edu.cn; chliu81@ustc.edu.cn

semiconductor laser absorption spectroscopy[12], differential optical absorption spectroscopy, and Fourier transform infrared spectroscopy[13,14]. Various studies have been conducted on HCHO, revealing a positive long-term trend in HCHO concentrations in most cities in East China[15,16] These concentrations are mainly influenced by secondary formation and vehicle exhaust[17]. However, these studies are primarily focused on major cities and well-developed regions, neglecting the examination of HCHO in West China because of less observation data than East China. The in-situ observation of HCHO requires labor and corollary equipment, making it challenging to investigate the distribution in a large region, especially in West China, such as Tibet.

The Tibet Autonomous Region is located in the western part of China and spans 78°–99°E longitude and 27.5°–36.5°N latitude, covering approximately one-eighth of China's total area. As the central part of the Qinghai-Tibet Plateau, Tibet's average elevation reaches 4000 m (as shown in Fig. 1B). The high altitude of Tibet and surrounding mountains, such as the Himalayas and Tanggula, form a barrier against pollution from India and East China. Due to its unique topography, Tibet maintains lower temperatures and significantly reduced annual temperature variations than East China. Low temperature and rough terrain have resulted in a sparser population, with only 3.66 million permanent people, primarily concentrated in river valleys. However, some pollutants can pass through this barrier and transfer to Tibet[18–20]. Carbonaceous aerosols can be transported into Tibet at altitudes of 4–6 km[21] or lifted through trans-Himalayan valleys[22]. With on-site monitoring, many events of increased O_3 have been observed in Tibet[23–25]. Tang et al. monitored the VOC concentration in urban areas and background areas in both North China and on the Qinghai-Tibet Plateau from 2012 to 2014 and 2020–2022 and found that the VOC concentration in urban areas on the plateau had risen by 2.5 times compared to the period of 2012–2014, which is comparable to the rise observed in North China[26]. This article provides us with a significant understanding of VOCs on the Qinghai-Tibet Plateau. Nevertheless, the temporal and spatial distribution of the data is not ideal due to limitations in the collection of station data. HCHO serves as an essential precursor of O_3 and VOCs reactive indicator, and it is imperative to understand the changes in HCHO VCD in Tibet. However, because of the limited number of available observation sites to HCHO, the assessment of HCHO concentrations in Tibet is restricted and intermittent.

Satellite-based remote sensing techniques can be utilized to effectively obtain long-term and large-scale HCHO concentrations, providing essential data support for understanding pollution causes and pollution prevention and control in Tibet. The Ozone Mapping and Profiler Suite (OMPS), launched in 2011, has maintained a high signal-to-noise ratio in its measured spectrum (>1000). This paper aims to analyze the inter-annual variation, seasonal characteristics, and main factors influencing HCHO in Tibet based on OMPS observations. Additionally, by integrating many auxiliary data, we provide a comprehensive analysis on the sources of the high HCHO concentration region we find in eastern region of Tibet.

Results and discussion

Spatial and temporal evolution characteristics of HCHO over Tibet

Based on the OMPS satellite, we retrieve tropospheric HCHO vertical column densities (VCD) in Tibet and its surrounding regions over nine years from 2013 to 2021. As shown in Fig. 1A, the nine-year average tropospheric HCHO VCD in Tibet from 2013 to 2021 is 2.17×10^{15} molec cm^{-2}, which is significantly lower than that observed in India, Nepal, and other South Asian countries. In consideration of population and geographical location, we divide Tibet into three regions: the western region, central region, and eastern region (marked in Fig. 1). We find that there are significant differences in HCHO distribution characteristics among three regions. The western region, characterized by sparse population and vegetation due to cold weather and rough terrain, exhibits the lowest tropospheric HCHO VCD, with a nine-year mean value of 1.80×10^{15} molec cm^{-2}. The central region and eastern region, housing the majority of Tibet's population, display higher tropospheric HCHO VCD compared to the western region, registering values of 1.97×10^{15} molec cm^{-2} and 2.78×10^{15} molec cm^{-2}, respectively.

From 2013 to 2021, the spatial distribution of tropospheric HCHO VCD in Tibet and surrounding regions remains nearly unchanged, and the eastern region consistently maintains the highest HCHO VCD (Fig. 2). However, the tropospheric HCHO VCD in Tibet is increasing, and the high-concentration of HCHO VCD area in the eastern region has significantly expanded. From 2018 to 2020, high-concentration of HCHO VCD area in the eastern region visibly diffuses to the central region. We calculate the monthly averaged tropospheric HCHO VCD in Tibet from 2013 to 2021 to investigate its monthly and inter-annual change trends (Fig. 3A). To maintain the correct character of the time series of tropospheric HCHO VCD, we discard the months in which more than 70% of the data are missing. The tropospheric HCHO VCD in Tibet presents significant and regular monthly variation characteristics, with the maximum value during June to August and the minimum value during November to January. The peak pattern of tropospheric HCHO VCD is consistent with the general variation characteristics in other studies[27]. To quantify the inter-annual variability of the tropospheric HCHO VCD, we use a linear model with sine and cosine functions of seasonality variation (Eq. (1)) to fit the monthly averaged HCHO data. The fitting parameter A of simulation function represents slope, and is used to estimate the annual growth rate of HCHO VCD. As shown in Fig. 3A, the model successfully captures the trend of the monthly averaged tropospheric HCHO VCD of Tibet. The simulated tropospheric HCHO VCD shows a strong correlation with the measured tropospheric HCHO VCD, with a correlation coefficient (R) of 0.76 and a low root mean square error (RMSE) of 0.36×10^{15} molec cm^{-2} (Table 1). The fitting results suggest a significant positive trend in the tropospheric HCHO VCD in Tibet, with a growth rate of 4.90×10^{13} molec cm^{-2} yr^{-1} from 2013 to 2021, almost 2.25% yr^{-1}. The increasing rate is much higher than those in the North China Plain and Yangtze River Delta, which are 1.80% yr^{-1} and 1.60% yr^{-1} from 2005 to 2016[28]. The trend is much closer to the average trend in the Indian continent, with a value of 2.40% yr^{-1} from 2005 to 2019[15]. The abnormally elevated tropospheric HCHO VCD at the third pole is unexpected because the tropospheric HCHO VCD in most of the world is declining.

Similarly, we investigate the long-term variation characteristics of tropospheric HCHO VCD over nine years in the western region, central region, and eastern region in Tibet applying same method. As shown in Fig. 3B–D, the tropospheric HCHO VCD in the western region and central region both follow similar monthly patterns, reaching a maximum in July and a minimum in December, which are the same as the trend in Tibet. The simulated tropospheric HCHO VCD correlates well with measured HCHO VCD in the western region ($R = 0.73$) and the central region ($R = 0.76$). The fitting results suggest significant increasing trend of the tropospheric HCHO VCD in western and central Tibet from 2013 to 2021, with annual growth rates of 2.53×10^{13} molec cm^{-2} yr^{-1} and 4.75×10^{13} molec cm^{-2} yr^{-1}, respectively. The HCHO VCD in central region increases faster than that in western region. As can be seen from Fig. 2, the boundary of high HCHO VCD area in the eastern region is gradually expanding and spreading to the central region, so this may be one reason why the annual growth rate of HCHO VCD in the central region is significantly higher than that in the western region.

In the eastern region of Tibet, the tropospheric HCHO VCD presents different monthly patterns from the other two regions and have no maximum or minimum in specific months. The simulated tropospheric HCHO VCD from the monthly fitting model maintains worse correlation with the measured HCHO results ($R = 0.58$). And we find the tropospheric HCHO VCD in eastern Tibet has a significant increasing trend with an annual growth rate of 6.06×10^{13} molec cm^{-2} yr^{-1}, 23.7% higher than the average trend in Tibet.

In addition, the nine-year temporal evolution of tropospheric HCHO VCD in the six major cities in Tibet, including Lhasa, Xigaze, Shannan, Nagqu, Nyingchi, and Qamdo, is also studied (Fig. 3E–J). Tropospheric

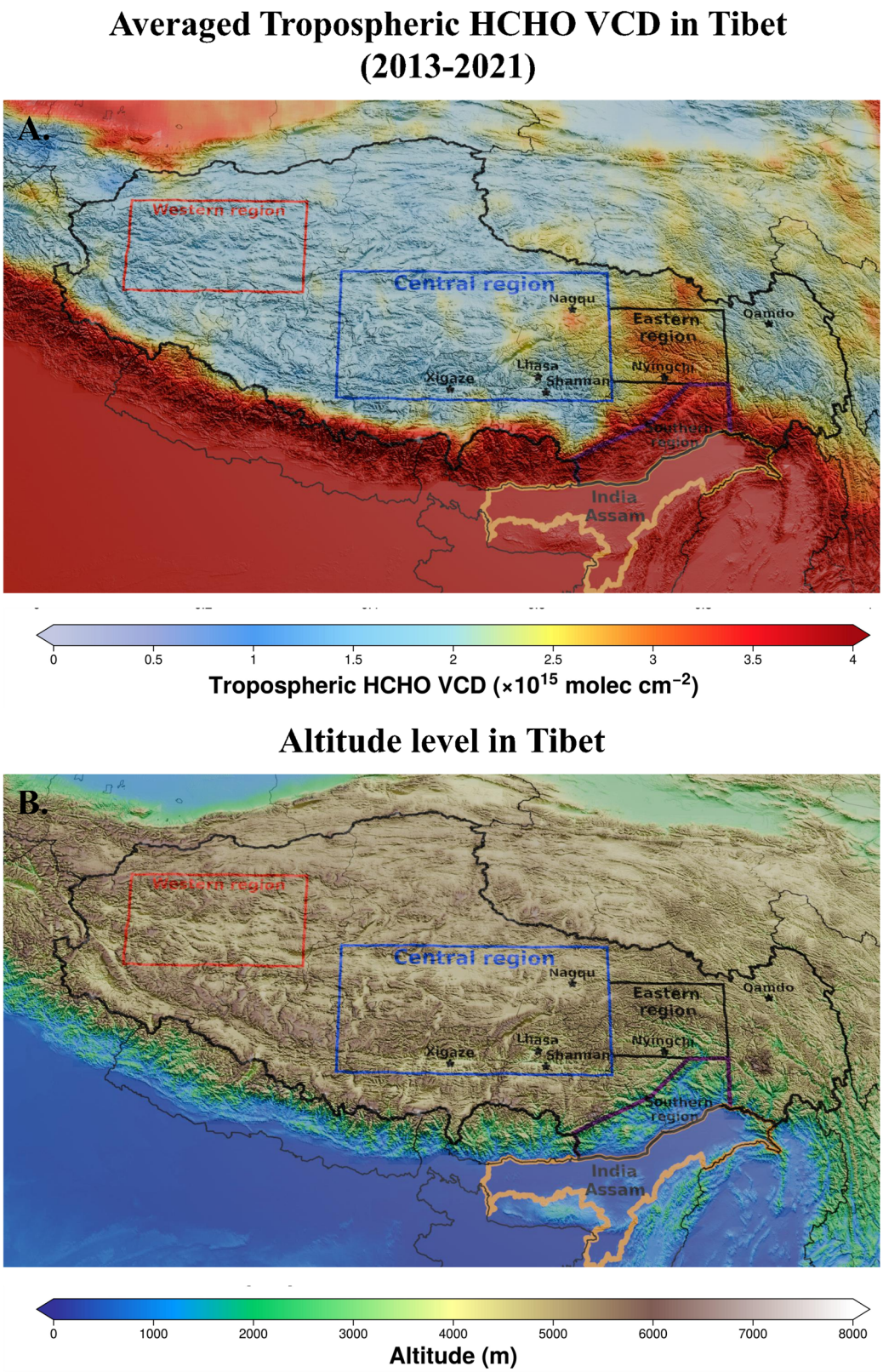

Fig. 1 | Spatial distribution of averaged tropospheric HCHO VCD from 2013 to 2021 and altitude of Tibet in 3D view. A Spatial distribution of averaged tropospheric HCHO VCD in Tibet from 2013 to 2021 in 3D view. **B** Altitude distribution map of Tibet in 3D view. The area framed by a thick black line is Tibet. The rectangles from left to right are the western region (red), central region (blue), and eastern region (black). The cities in figure from left to right are Xigaze, Lhasa, Shannan, Nagqu, Nyingchi, and Qamdo. For follow-up studies, we also show the approximate extent of southern region (violet) in Tibet with lower altitude and further south India assam (orange).

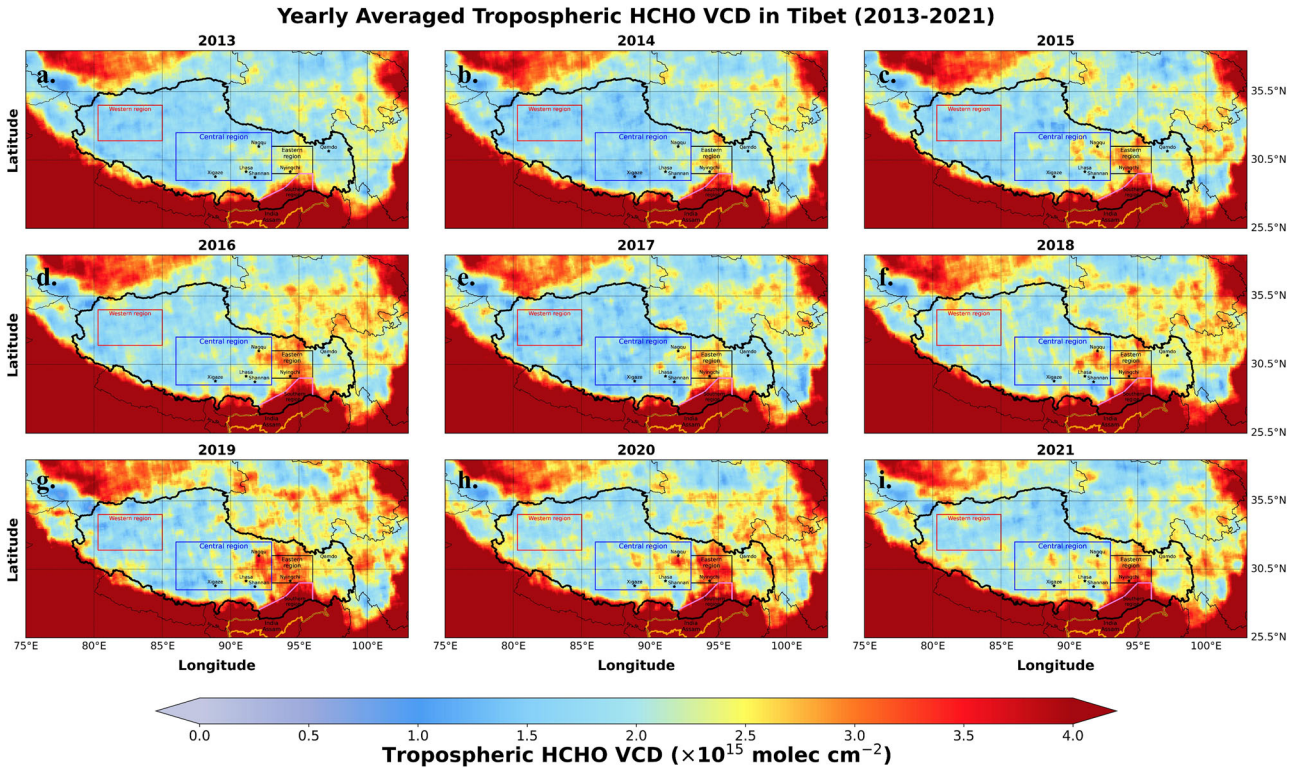

Fig. 2 | Spatial distribution of the yearly averaged tropospheric HCHO VCD in Tibet from 2013 to 2021. The yearly averaged tropospheric HCHO VCD in Tibet for each year. The labels of the rectangles and marks are the same as those in Fig. 1.

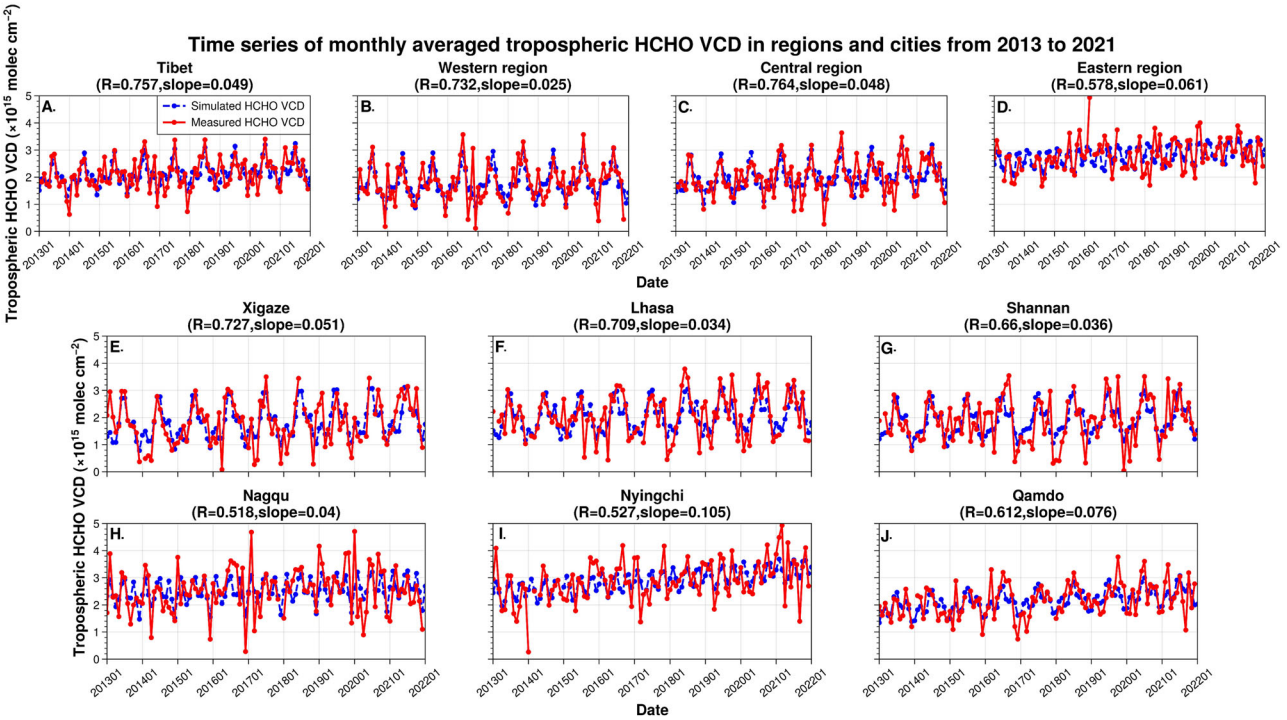

Fig. 3 | Time series of monthly averaged tropospheric HCHO VCD in Tibet from 2013 to 2021. Time series of monthly averaged tropospheric HCHO VCD in (**A**) the whole Tibet, (**B–D**) three regions and (**E–J**) six major cities from 2013 to 2021. The red solid line represents measured monthly average tropospheric HCHO VCD. The blue dot line represents the simulated tropospheric HCHO VCD. The slope is parameter A in Eq. (1) and represents the annual growth rate of HCHO VCD.

HCHO VCD within ±0.5° latitude and longitude around the city center is averaged as the HCHO VCD of the city. Four cities are located in the central region, including Lhasa, Xigaze, Shannan, and Nagqu. The mean tropospheric HCHO VCD in Lhasa (2.07×10^{15} molec cm^{-2}), the provincial capital of Tibet, is higher than that in Xigaze (1.81×10^{15} molec cm^{-2}) and Shannan (1.89×10^{15} molec cm^{-2}), and lower than that in Nagqu (2.54×10^{15} molec cm^{-2}), which is close to the eastern region. The tropospheric HCHO VCD in Nagqu is 27.60% higher

Table 1 | The mean tropospheric HCHO VCD and annual growth rates and the correlation coefficients between the measured and simulated HCHO data (R) in three regions and six cities

Region and city name	Mean tropospheric HCHO VCD (10^{15} molec cm^{-2})	Annual growth rate of tropospheric HCHO VCD (10^{13} molec cm^{-2} yr^{-1})	*R*	RMSE (10^{15} molec cm^{-2})
Tibet	2.17	4.90	0.76	0.36
Western Region	1.79	2.53	0.73	0.47
Central Region	1.99	4.75	0.76	0.40
Xigaze	1.81	5.08	0.73	0.56
Lhasa	2.07	3.39	0.71	0.55
Shannan	1.89	3.57	0.66	0.61
Nagqu	2.54	4.03	0.52	0.70
Eastern Region	2.80	6.06	0.58	0.48
Nyingchi	2.90	10.51	0.53	0.64
Qamdo	2.17	7.64	0.61	0.48

All correlation coefficient (R) is significant ($p < 0.01$).

than the mean HCHO VCD of the central region. Despite different levels of HCHO VCD, the tropospheric HCHO VCD in four cities all have increasing trend (Fig. 3 and Table 1). The annual growth rates of these four cities are 3.39×10^{13} molec cm^{-2} yr^{-1}, 5.08×10^{13} molec cm^{-2} yr^{-1}, 3.57×10^{13} molec cm^{-2} yr^{-1} and 4.03×10^{13} molec cm^{-2} yr^{-1}, respectively. Among them, the annual growth rate in Lhasa is the lowest, followed by Shannan. Although tropospheric HCHO VCD in Xigaze is lowest, its annual growth rate is highest in the four cities over the central region. Nyingchi is located on the southern boundary of the eastern region, and both its tropospheric HCHO VCD and annual growth rate of HCHO VCD are the highest among the six selected cities, reaching 2.90×10^{15} molec cm^{-2} and 10.51×10^{13} molec cm^{-2} yr^{-1}, respectively. Qamdo is located east of the eastern region and has a faster annual growth rate of HCHO VCD than cities in the central region, reaching 7.64×10^{13} molec cm^{-2} yr^{-1}. We conclude that tropospheric HCHO VCD and their annual growth rates in cities around the eastern part are higher. Besides, compared to other cities, the RMSE in Nagqu and Nyingchi are also highest among six cities. The reasons will be discussed in Sect 3.2 and Sect 3.3. Details of the mean tropospheric HCHO VCD, annual growth rates, the correlation coefficients (R) and RMSE between the measured and simulated HCHO VCD are listed in Table 1.

According to previous studies, HCHO VCD often exhibit strong seasonal characteristics[29,30]. The distribution map and boxplots of seasonal average tropospheric HCHO VCD for nine years from 2013 to 2021 in Tibet are shown in Fig. 4A, B, respectively. We find that the tropospheric HCHO VCD shows different seasonal variations in each region in Tibet. In the central region and western region, the tropospheric HCHO VCDs vary significantly with seasons, with maximum values in summer and minimum values in winter. However, the seasonal variation in the eastern part is not apparent, and the tropospheric HCHO VCD always maintains high levels throughout all seasons. Among the six cities, Lhasa, Xigaze, and Shannan, located in central Tibet, display the expected seasonal cycle: high tropospheric HCHO VCD occurs in summer, and low tropospheric HCHO VCD is observed in winter. The summer average tropospheric HCHO VCD is highest and winter average levels are lowest in winter in Nagqu and Qamdo, while the seasonal variations are insignificant. In Nyingchi, the city in eastern Tibet, the tropospheric HCHO VCD maintain high values in all four seasons without significant seasonal features. In contrast to previous studies, the seasonal pattern in eastern Tibet is abnormal, we explore the potential reasons behind the deviation and the probable reason is discussed below.

Factors influencing the HCHO concentration in Tibet

Many factors influence the generation of HCHO[31–35]. Based on studies identifying significant influencing factors for HCHO VCD, we select a few factors more likely to affect HCHO concentration in Tibet.

The first factor considered is temperature. To investigate this potential influence, we conduct the spatial correlation analysis between monthly surface temperature data from ERA5 and monthly averaged tropospheric HCHO VCD from 2013 to 2021. This operation is performed on every $0.1° \times 0.1°$ grid, and we generate a spatial distribution map based on the acquired correlation coefficients (Fig. 5A). The results show that most areas in Tibet's central and western regions have a correlation coefficient of approximately 0.6, indicating that tropospheric HCHO VCD in these grids are strongly dependent on temperature. Therefore, we conclude that temperature is a significant factor influencing the HCHO concentration in Tibet's western region and central region. However, tropospheric HCHO VCD in the eastern region has no relationship with temperature.

Next, we calculate the mean population densities within a ±0.5°grid of the cities same as above based on the population data from the Gridded Population of the World v4 (GPWv4) and plot them with averaged tropospheric HCHO VCD from 2013 to 2021 (Fig. 5B). We find that there appears to be an inverse relationship between population density and HCHO concentration in Tibet, contrary to the previous study where HCHO concentrations have a positive trend with population in eastern China[7]. For instance, the population density in Lhasa, the provincial capital, is much higher (48.27 people km^{-2}) than that in Nyingchi (7.20 people km^{-2}) and Nagqu (9.00 people km^{-2}) cities. The average tropospheric HCHO VCD from 2013 to 2021 in Lhasa is 2.07×10^{15} molec cm^{-2}, which is significantly lower than that in Nyingchi (2.90×10^{15} molec cm^{-2}) and Nagqu (2.54×10^{15} molec cm^{-2}). These results suggest that population density is not the primary factor influencing HCHO concentrations in urban areas of Tibet.

HCHO can be produced from photochemical oxidation of isoprene emitted by vegetation, which is an essential source of HCHO on a global scale. We use the Normalized Difference Vegetation Index (NDVI) to reflect the biogenic emission intensity of HCHO. As shown in Fig. 5C, the NDVI is very low in most parts of Tibet, less than 0.2. Only in southern region and part of the eastern region the NDVI is high because of low altitude. We use the same method as what we do when we analyze HCHO VCD-temperature correlation. The correlation map (Supplementary Fig. 1) shows that HCHO VCD is positively correlated with NDVI in most of western and central regions. The correlation coefficients between HCHO VCD and NDVI are low in most area of Tibet, except central region where correlation coefficient can reach 0.6. Vegetation-emitted HCHO has an obvious seasonal pattern, reaching its highest in summer and lowest in winter owing to more vigorous plant growth and strong oxidation processes in summer, like seasonal variations in NDVI (Supplementary Fig. 2). Similar seasonal variation is one reason why HCHO VCD is highly correlated with NDVI in central region. NDVI in eastern region have apparently seasonal variation. However, the winter mean tropospheric HCHO VCD in the eastern region remains similar to the summer mean value. And we find no correlation between HCHO VCD and the NDVI in the eastern region (Supplementary Fig. 1). Moreover, the annual variation of NDVI in the eastern region is small (Supplementary Fig. 3), which is inconsistent with the characteristics of HCHO VCD increasing year by year. These results indicate that biogenic emission is a non-negligible source of HCHO VCD in Tibet but not the leading cause of the unusual long-term increases and abnormal seasonal trends of HCHO VCD in the eastern region.

The above results suggest that the local temperature plays a significant role in influencing tropospheric HCHO VCD in the western region and central region, and NDVI in central region has obvious influence on HCHO

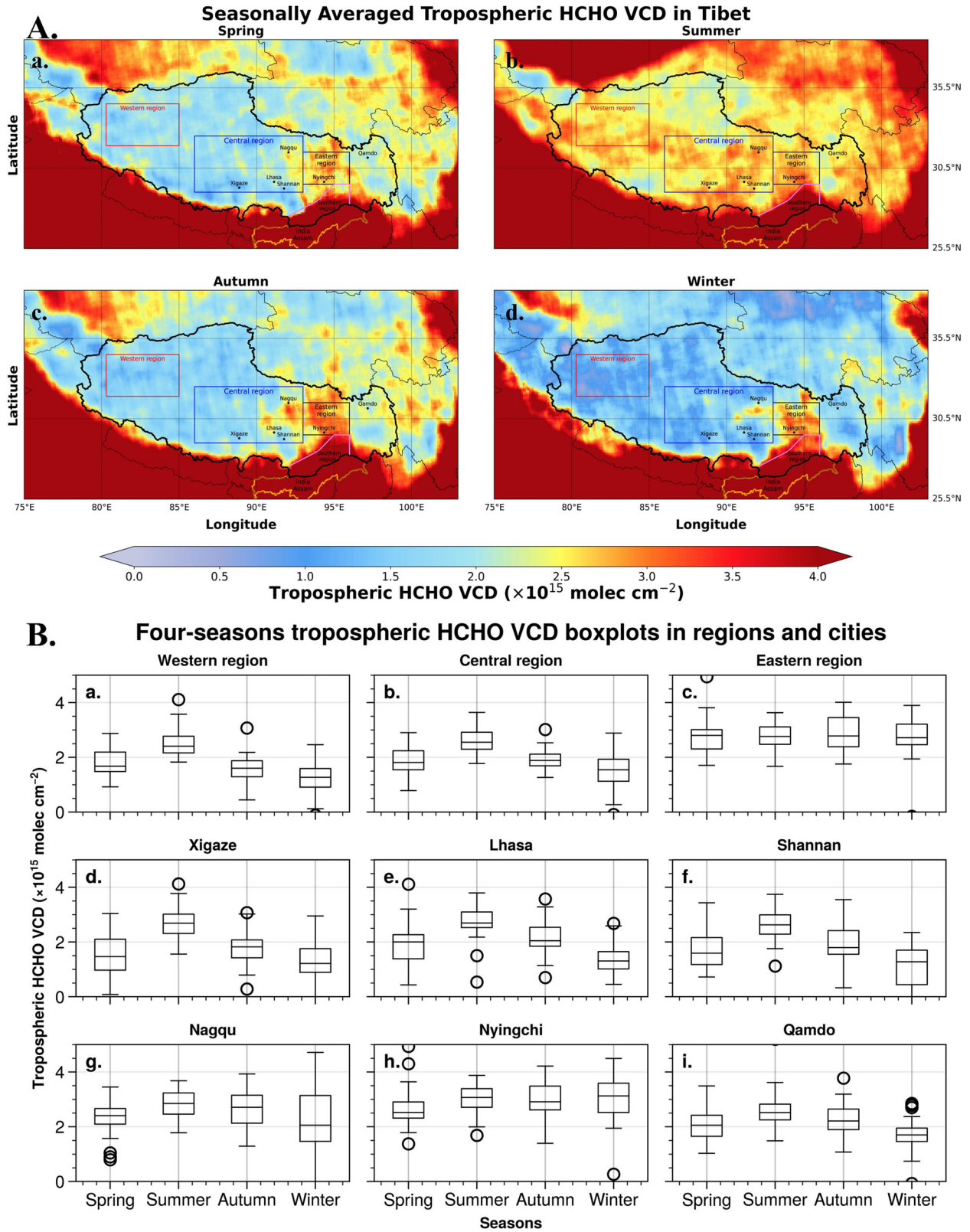

Fig. 4 | Distribution of seasonally tropospheric HCHO averaged tropospheric HCHO VCD in Tibet. A Seasonally averaged tropospheric HCHO VCD in Tibet. **B** Four-seasons tropospheric HCHO VCD in (**a**–**c**) three regions and (**d**–**i**) six cities. We average HCHO VCD for the same season from 2013 to 2021.

VCD. But unusual long-term increases and abnormal seasonal trends of high HCHO VCD in the eastern region is not related to any local element. Instead, it is apparent that external factors of some nature exert an influence on HCHO VCD in the eastern region.

Unexpected VOC transport from India to Tibet through the Assam Plain – Yarlung Zangbo Grand Canyon

The Yarlung Zangbo River Grand Canyon, situated in the southern part of the eastern region, serves as a crucial link between the Qinghai-Tibet Plateau

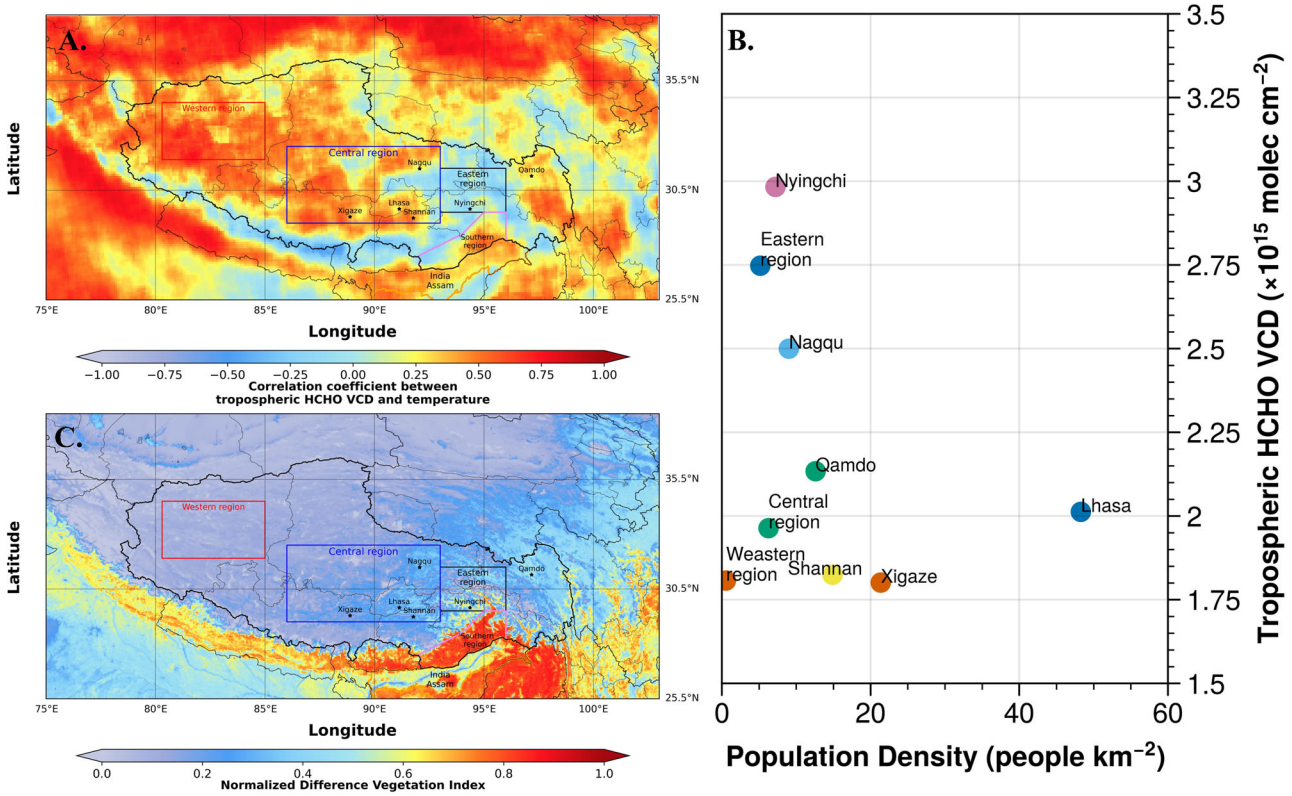

Fig. 5 | Correlation between HCHO VCD and its possible influencing factors. **A** Spatial distribution of correlation between tropospheric HCHO VCD and temperature in the Tibet from 2013 to 2021. **B** The relationship between population density and average tropospheric HCHO VCD in major cities and regions of Tibet from 2013 to 2021. **C** Spatial distribution map of NDVI in Tibet from 2013 to 2021.

and the Assam Plain of India, spanning an elevation of ~2000 to 4000 meters above sea level. Previous studies have confirmed the transport of persistent organic pollutants to the Qinghai-Tibet Plateau along the Yarlung Zangbo River valley[36]. However, there has been no research demonstrating a pathway for formaldehyde (HCHO) or VOCs to enter the Qinghai-Tibet Plateau via the Yarlung Zangbo River valley.

As shown in Fig. 1A, the tropospheric HCHO VCD near the Yarlung Zangbo River valley is higher than that in the surrounding area. To preliminarily access the possibility of HCHO transport from southern Tibet to the eastern region, we analyze the influence of the wind field on HCHO VCD in eastern region. Utilizing ERA5 wind field data (1000 m above the ground) in the eastern region, we calculate the dot product between the wind vector and normal vector at the southern boundary of the eastern region. Then, we segment the dot product values and average the tropospheric HCHO VCD over those days that have dot product within the same segment. The averaged tropospheric HCHO VCD corresponding to the dot product values is shown in Fig. 6A. The positive values of the dot product indicate that HCHO is transported into the eastern region though the southern boundary and opposite for negative values. The tropospheric HCHO VCD in the eastern region increases significantly with increasing dot product value, indicating a significant positive correlation between tropospheric HCHO VCD and the wind vector in the eastern region. The results suggest that HCHO transportation from the southern Tibet has critical effects on HCHO concentrations in the eastern region of Tibet.

Furthermore, to find the source of this critical effect. we conduct backward trajectory clustering analysis on the point located in the Yarlung Zangbo River Grand Canyon and southern boundary of eastern region from 2013 to 2021 using wind fields at 1000 m above ground (Fig. 6B). In the four seasons, more than 60% of backward trajectories originate from India Assam, and this proportion increases to 75% in summer and autumn. Combining the above two points, we consider that the high HCHO VCD in eastern region is mainly influenced by India assam. We conclude that the emitted HCHO or its precursor VOC from India Assam are transported to Tibet through the Yarlung Zangbo Grand Canyon, polluting the atmosphere in the eastern region and southern region.

To elucidate the HCHO characteristics of the India Assam and southern regions in the transport pathway, we plot the monthly averaged tropospheric HCHO VCD from 2013 to 2021 for both areas compared with the HCHO result in the eastern region simultaneously (Fig. 7A). The nine-year averaged tropospheric HCHO VCD in India Assam and the southern and eastern regions in Tibet are 1.23×10^{16} molec cm^{-2}, 6.56×10^{15} molec cm^{-2} and 2.78×10^{15} molec cm^{-2}, respectively. The HCHO value decreases along the transport pathway, and the probable reasons are the increase in terrain height and HCHO sinks. In both the southern region and India Assam, the tropospheric HCHO VCD peaks in March and April. Combined with TROPOMI CO data from 2019 to 2021 (Fig. 7B), we find that the CO VCD in both the southern region and India Assam also reaches its peak in March and April of each year. The apparent relationship between CO and HCHO indicates that the HCHO VCD in these two regions is significantly affected by anthropogenic sources, such as fires, factories, and vehicles. To investigate this result further, we use the MODIS fire product to statistically analyze the monthly mean Fire Radiative Power (FRP) values in the southern region and India Assam from 2013 to 2022 (Fig. 7C). In March and April, the Fire Radiative Power (FRP) in India Assam and the southern region reaches its peak, much higher than that in other months. The Fire Radiative Power (FRP) in India Assam is much higher than that in the southern region. Fires often release much CO and VOCs, which have longer lifetime than VOCs emitted from familiar sources and are more challenging to decompose[37]. The low temperature of the Qinghai-Tibet Plateau impedes the conversion of VOCs into HCHO, increasing the likelihood that these VOCs enter the Qinghai-Tibet Plateau through the Yarlung Zangbo River Canyon, leading to HCHO pollution. This transport influences the concentration of HCHO in the eastern region and causes secondary pollution by O_3. It is

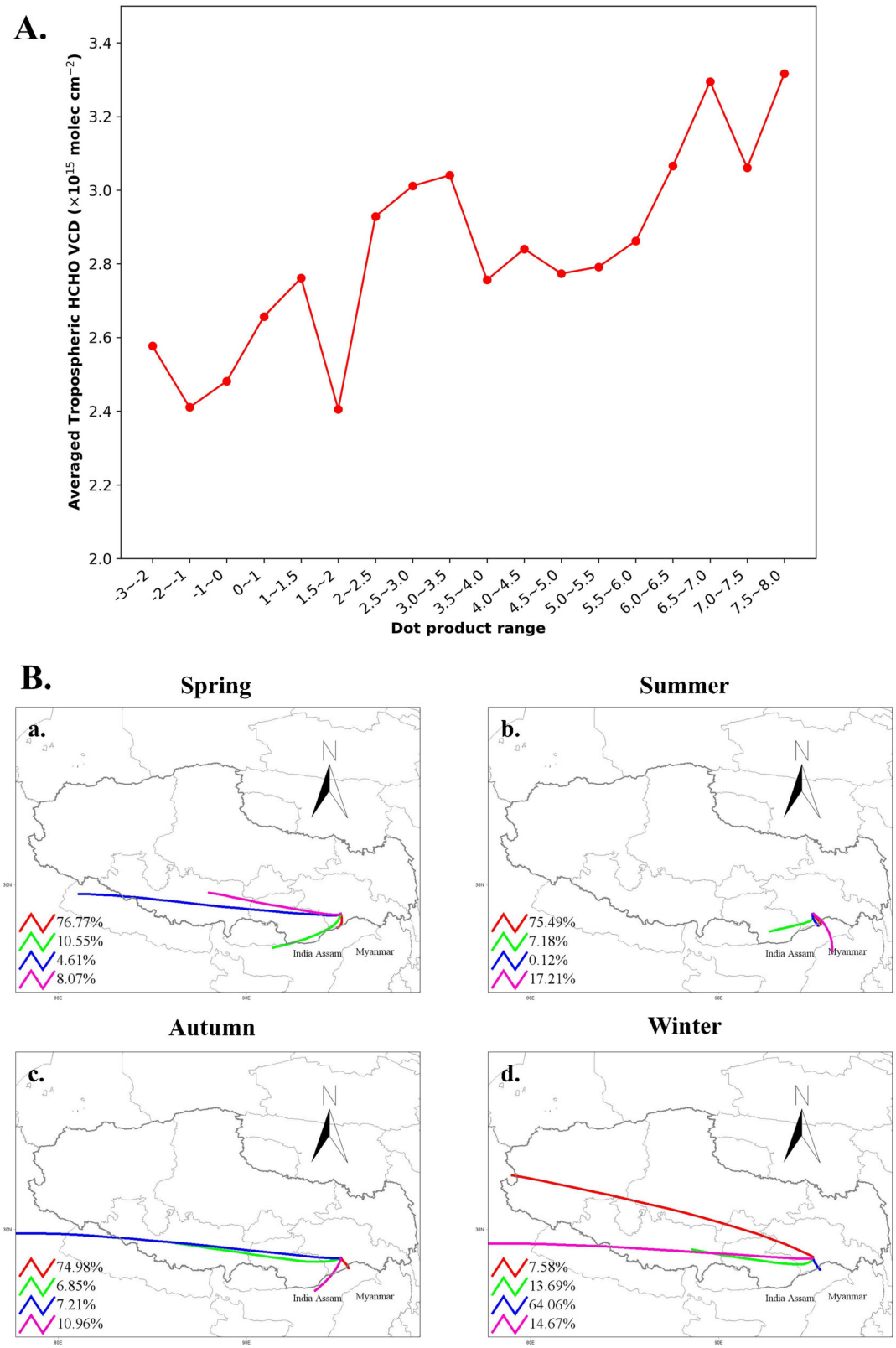

Fig. 6 | Relationship between HCHO VCD in the eastern region and transportation, and source of transportation. A Relationship between the average HCHO VCD in the eastern region and the dot product of the wind vector and the normal vector at the southern boundary of the eastern region. The average HCHO VCD in the corresponding dot product segment is the red solid line. **B** Backward trajectory of the southern boundary points in the four seasons of the eastern region from 2013 to 2021. The backward trajectory (−1 day) and proportion of each backward trajectory in a Spring, b Summer, c Autumn, and d Winter. The total proportion of the four backward trajectories in one map is 100%, and the number next to the line is the proportion of the corresponding backward trajectory.

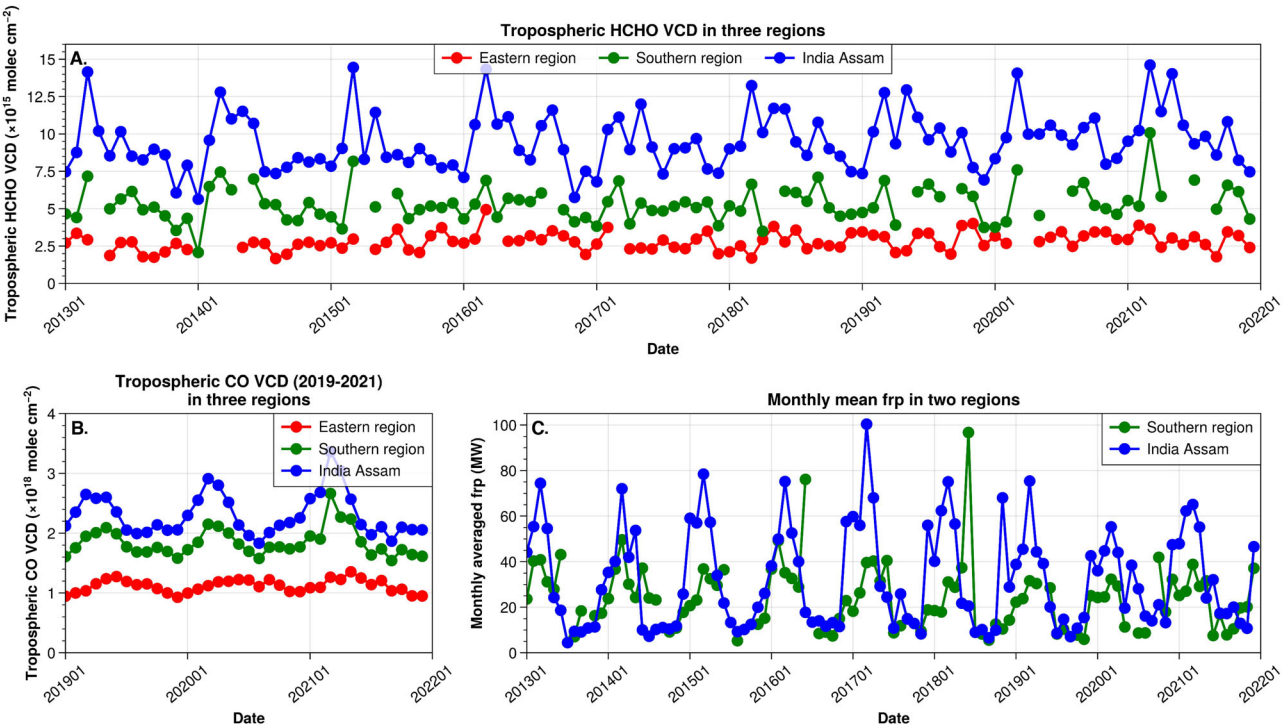

Fig. 7 | Comparsion of HCHO VCD, CO VCD and monthly mean frp among eastern region, southern region and india assam. A Time trend of monthly mean tropospheric HCHO VCD in the southern region (green line) and India Assam (blue line) compared with the eastern region (red line) from 2013 to 2021. **B** Time trend of monthly mean CO total columns in the eastern region (red), southern region (blue), and India Assam (green) from 2019 to 2021. **C** Time trends of monthly mean Fire Radiative Power (FRP) in the southern region (green) and India Assam (blue) from 2013 to 2021.

clearly shown that the tropospheric O_3 VCD along the Yarlung Zangbo River Canyon and eastern region in Tibet is significantly higher than that in the western and central regions (Supplementary Fig. 4). The pollution and health hazards caused by the transport should be continuously monitored.

Methods

OMPS HCHO measurements

OMPS-NM is one of the instrument packages of the OMPS, launched on the Suomi-NPP satellite on October 28, 2011. The Suomi-NPP satellite is a polar sun-synchronous satellite with an average altitude of 824 km, crossing the equator at 13:30 local time at the ascending node every day. OMPS-NM uses a single grating and a 340 × 740 pixels CCD, with a 300–370 nm spectral range. The signal-to-noise ratio of the OMPS-NM sensor can reach 2000:1 or above, with a spatial resolution of 50 km × 50 km[38].

The tropospheric HCHO VCD we use in this study are calculated mainly following two steps: slant column density (SCD) retrieval and air mass factor calculation. The SCD is retrieved based on the fundamental optical differential spectroscopy method[39]. Given the characteristics of low HCHO concentrations and complex terrain in Tibet, we optimize the SCD retrieval model to reduce interference from strongly absorbing gases and aerosol scattering and to improve retrieval accuracy. We utilized a priori HCHO of the overpass times of the OMPS satellite in Tibet in calculating the air mass factor. In this study, we filter the data with cloud fractions greater than 0.5 and root-mean-square values greater than 0.001 to reduce retrieval uncertainty.

TROPOMI CO and O_3

The TROPOMI instrument is mounted on the Sentinel-5 precursor satellite, which operates on a near-polar, sun-synchronous orbit at an altitude of 824 km and repeats its orbit every 17 days. It flies over the equator daily at 13:30 local time at the ascending node. TROPOMI consists of four spectrometers (UV, UVIS, NIR, and SWIR) covering eight nonoverlapping and noncontinuous spectral bands from 270 to 2385 nm. The CO and O_3 data are retrieved from band 7 and band 3 spectra, respectively. The wavelength range of band 7 is 2300–2342 nm. The data in this band are acquired by the CCD of the SWIR spectrometer, which has 480 × 450 pixels with a spectral resolution of 0.23 nm[40]. The wavelength range of band 3 is 305–400 nm, with a spectral range of 0.5 nm. The spatial resolutions of the two spectrometers are 7 × 7 km and 7 × 3.5 km (since 6 August 2019, the resolutions have improved to 5.5 km × 7 km and 5.5 km × 3.5 km).

Because of the higher spatial resolution but shorter time coverage, we use trace gas data from TROPOMI as auxiliary data and validate some conclusions.

Meteorological data from ERA5 reanalysis products

ECMWF Reanalysis v5 (ERA5) is the latest global reanalysis dataset from the European Centre for Medium-Range Weather Forecasts (ECMWF), which replaces ERA-Interim. Based on the 4D-Var data assimilation method and 41r2 cycle of the Integrated Forecasting System (IFS), ERA5 provides long-term global atmospheric data of various quantities, such as absolute temperature, relative humidity, and wind speed, for selectable regions[41]. Its unique advantages lie in its high temporal and spatial resolutions, providing finely gridded data at a spatial resolution of 31 × 31 km and hourly temporal resolution, with a vertical resolution of 137 levels from 0.01 hPa to the surface, offering more details of atmospheric parameters.

MODIS fire products and vegetation index products

The Moderate Resolution Imaging Spectroradiometer (MODIS) was launched on the Terra platform in December 1999 as part of NASA's Earth Observing System (EOS). The MODIS instrument, which began collecting image data in February 2000, generates numerous land surface products to meet the goals of NASA's Earth Science Enterprise.

MODIS Fire Products are designed to provide information for global change science and practical applications[42]. They are generated using a contextual algorithm. The algorithm applies thresholds to the brightness

temperatures of the mid-IR and thermal IR channels of the MODIS instrument. During satellite overpasses, active fire is mapped and screened at a resolution of 1 km. Under very good observation condition, small fires of 100 m^2 or even 50 m^2 can be detected though the product provide data with 1000 m pixel size.

MODIS Vegetation Index Products provide two vegetation indices: NDVI and EVI, derived from atmospherically-corrected reflectance in the red, near-infrared, and blue wavebands. In this study, we use NDVI to explore the relationship between HCHO VCD and vegetation in Tibet.

GPWv4

GPW (Gridded Population of World) collection provides a simulated population distribution (counts and densities) on a continuous global raster surface. The purpose of GPW is to provide a spatially disaggregated population layer that is compatible with data sets from social, economic, and Earth science disciplines, and remote sensing. its primary inputs are census tabulations and the corresponding geographic boundaries. For GPWv4, it uses the highest precision population and housing census results from 2005 to 2014 as input and extrapolates them to obtain population estimates for each five-year period from 2000 to 2020, ultimately providing a gridded output with a precision of 30 arcseconds.

Interannual change simulation

To investigate the annual growth of HCHO in Tibet, we establish a model to simulate tropospheric HCHO VCD:

$$Y = An/12 + B + \sum_{i=1}^{3} a_i \sin\left(\frac{2\pi in}{12}\right) + \sum_{i=1}^{3} b_i \cos\left(\frac{2\pi in}{12}\right) \quad (1)$$

where Y is the monthly average HCHO VCD, n is the number of months from January 2013, $An/12+B$ represents the linear trend of monthly average tropospheric HCHO VCD, A represents the annual growth of HCHO, and B is the intercept. $\sum_{i=1}^{3} a_i \sin(2\pi in/12) + \sum_{i=1}^{3} b_i \cos(2\pi in/12)$ represents the seasonal cyclic trend of monthly average HCHO VCD, with a_i and b_i being seasonal cyclic variation coefficients. At the same time, we also calculate correlation coefficient (R) and RMSE between simulated HCHO VCD and measured HCHO VCD using the following two formulas to represent goodness of this model:

$$R = \frac{\sqrt{\sum_{n=1}^{N}(V_{\mathrm{mea},n} - \overline{V_{\mathrm{mea}}})(V_{\mathrm{sim},n} - \overline{V_{\mathrm{sim}}})}}{\sqrt{\sum_{n=1}^{N}(V_{\mathrm{mea},n} - \overline{V_{\mathrm{mea}}})^2}\sqrt{\sum_{n=1}^{N}(V_{\mathrm{sim},n} - \overline{V_{\mathrm{sim}}})^2}} \quad (2)$$

$$RMSE = \sqrt{\frac{\sum_{n=1}^{N}(V_{\mathrm{sim},n} - V_{\mathrm{mea},n})^2}{N}} \quad (3)$$

where, V_{mea} is the measured HCHO VCD. V_{sim} is the simulated HCHO VCD. The variable with the horizontal line above represents the mean value of the variable. N is total month number from 2013 to 2021.

Data availability

The HCHO VCD and O_3 concentration data and codes are available from the corresponding author (C.L.) upon request, and TROPOMI CO concentration data can be obtained from ESA Sentinel Online (https://sentinels.copernicus.eu/web/sentinel/data-products/-/asset_publisher/fp37fc19FN8F/content/sentinel-5-precursor-level-2-carbon-monoxide). ERA5 is available at the ECMWF website (https://www.ecmwf.int/en/forecasts/dataset/ecmwf-reanalysis-v5). The MODIS fire product and EVI data are accessible at the MODIS website (https://modis.gsfc.nasa.gov/data/dataprod/). GPWv4 is available from the Socioeconomic Data and Applications Center (https://sedac.ciesin.columbia.edu/data/collection/gpw-v4).

Received: 25 September 2023; Accepted: 27 February 2024;
Published online: 14 May 2024

References

1. Kleinman, L. I. Seasonal dependence of boundary layer peroxide concentration: the low and high NO x regimes. *J. Geophys. Res. Atmosp.* **96**, 20721–20733 (1991).
2. Steinfeld, J. I. Atmospheric chemistry and physics: from air pollution to climate change. *Environ. Sci. Policy Sustain. Dev.* **40**, 26–26 (1998).
3. Booker, F. et al. The ozone component of global change: potential effects on agricultural and horticultural plant yield, product quality and interactions with invasive species. *J. Integr. Plant Biol.* **51**, 337–351 (2009).
4. Nel, A. Air pollution-related illness: effects of particles. *Science* **308**, 804–806 (2005).
5. Stephens, E. R. The formation, reaction, and properties of peroxyacyl nitrates (PANs) in photochemical air pollution. *Adv. Environ. Sci. Technol.* **1**, 119–146 (1969).
6. World Health Organization. *WHO Guidelines for Indoor Air Quality: Selected Pollutants.* (World Health Organization. Regional Office for Europe, Copenhagen, 2010).
7. Su, W. et al. Inferring global surface HCHO concentrations from multisource hyperspectral satellites and their application to HCHO-related global cancer burden estimation. *Environ. Int.* **170**, 107600 (2022).
8. Hong, Q. et al. Evaluating the feasibility of formaldehyde derived from hyperspectral remote sensing as a proxy for volatile organic compounds. *Atmos. Res.* **264**, 105777 (2021).
9. Javed, Z. et al. Ground-based MAX-DOAS observations of CHOCHO and HCHO in Beijing and Baoding, China. *Remote Sens.* **11**, 1524 (2019).
10. Salas, L. J. & Singh, H. B. Measurements of formaldehyde and acetaldehyde in the urban ambient air. *Atmos. Environ.* **20**, 1301–1304 (1986).
11. Inomata, S. et al. Determination of formaldehyde mixing ratios in air with PTR-MS: laboratory experiments and field measurements. *Atmos. Chem. Phys.* **8**, 273–284 (2008).
12. Fischer, H., Bergamaschi, P., Wienhold, F. G., Zenker, J. T. & Harris, G. W. Development and application of multilaser TDLAS instruments for ground-based, shipboard, and airborne measurements of trace gas species in the atmosphere. in *Application of Tunable Diode and Other Infrared Sources for Atmospheric Studies and Industrial Process Monitoring* vol. 2834 130–141 (SPIE, 1996).
13. Franco, B. et al. Retrievals of formaldehyde from ground-based FTIR and MAX-DOAS observations at the Jungfraujoch station and comparisons with GEOS-Chem and IMAGES model simulations. *Atmos. Meas. Tech.* **8**, 1733–1756 (2015).
14. Javed, Z. et al. Investigating the impacts of the COVID-19 lockdown on trace gases using ground-based MAX-DOAS observations in Nanjing, China. *Remote Sens.* **12**, 3939 (2020).
15. Bauwens, M., Verreyken, B., Stavrakou, T., Müller, J. & De Smedt, I. Spaceborne evidence for significant anthropogenic VOC trends in Asian cities over 2005–2019. *Environ. Res. Lett.* **17**, 015008 (2022).
16. De Smedt, I. et al. Trend detection in satellite observations of formaldehyde tropospheric columns. *Geophys. Res. Lett.* **37**, 18 (2010).
17. Ling, Z., Zhao, J., Fan, S. & Wang, X. Sources of formaldehyde and their contributions to photochemical O3 formation at an urban site in the Pearl River Delta, southern China. *Chemosphere* **168**, 1293–1301 (2017).
18. Cong, Z. et al. Historical trends of atmospheric black carbon on Tibetan Plateau as reconstructed from a 150-year lake sediment record. *Environ. Sci. Technol.* **47**, 2579–2586 (2013).
19. Lin, H. et al. First measurement of atmospheric mercury species in Qomolangma Natural Nature Preserve, Tibetan Plateau, and evidence oftransboundary pollutant invasion. *Atmos. Chem. Phys.* **19**, 1373–1391 (2019).

20. Liu, J. et al. High contribution of south asian biomass burning to southeastern tibetan plateau air: new evidence from radiocarbon measurement. *Environ. Sci. Technol. Lett.* **8**, 1026–1031 (2021).
21. Li, J., He, Q., Jin, L. & Ge, X. Three-dimensional distribution of dust aerosols over the Tarim Basin and the Tibet Plateau during 2007–2021 derived from CALIPSO lidar observations. *J. Clean. Prod.* **400**, 136746 (2023).
22. Yuan, Q. et al. In situ observations of light-absorbing carbonaceous aerosols at Himalaya: analysis of the South Asian sources and trans-Himalayan valleys transport pathways. *J. Geophys. Res. Atmos.* **125**, e2020JD032615 (2020).
23. Bian, J., Yan, R., Chen, H., Lü, D. & Massie, S. T. Formation of the summertime ozone valley over the Tibetan Plateau: The Asian summer monsoon and air column variations. *Adv. Atmos. Sci.* **28**, 1318–1325 (2011).
24. Chen, Y. et al. Spatiotemporal variations of surface ozone and its influencing factors across Tibet: a Geodetector-based study. *Sci. Total Environ.* **813**, 152651 (2022).
25. Yin, X. et al. Surface ozone at Nam Co in the inland Tibetan Plateau: variation, synthesis comparison and regional representativeness. *Atmos. Chem. Phys.* **17**, 11293–11311 (2017).
26. Tang, G. et al. The urgent need to control volatile organic compound pollution over the Qinghai-Tibet Plateau. *Iscience* **25**, 12 (2022).
27. Zhang, C. et al. Satellite UV-Vis spectroscopy: implications for air quality trends and their driving forces in China during 2005–2017. *Light Sci. Appl.* **8**, 100 (2019).
28. Shen, L. et al. The 2005–2016 trends of formaldehyde columns over China observed by satellites: increasing anthropogenic emissions of volatile organic compounds and decreasing agricultural fire emissions. *Geophys. Res. Lett.* **46**, 4468–4475 (2019).
29. Palmer, P. I. et al. Quantifying the seasonal and interannual variability of North American isoprene emissions using satellite observations of the formaldehyde column. *J. Geophys. Res. Atmos.* **111**, D12 (2006).
30. Sun, Y. et al. Mapping the drivers of formaldehyde (HCHO) variability from 2015 to 2019 over eastern China: insights from Fourier transform infrared observation and GEOS-Chem model simulation. *Atmos. Chem. Phys.* **21**, 6365–6387 (2021).
31. Su, W. et al. An improved TROPOMI tropospheric HCHO retrieval over China. *Atmos. Meas. Tech.* **13**, 6271–6292 (2020).
32. Huang, C. et al. Spatial and temporal distribution of HCHO and its pollution sources based on satellite remote sensing: a case study of the Yangtze River Economic Belt. *Environ. Res. Commun.* **5**, 075014 (2023).
33. Fan, J. et al. Spatiotemporal variations and potential sources of tropospheric formaldehyde over eastern China based on OMI satellite data. *Atmos. Pollut. Res.* **12**, 272–285 (2021).
34. Zhu, S. et al. Spatiotemporal variations in satellite-based formaldehyde (HCHO) in the Beijing-Tianjin-Hebei region in China from 2005 to 2015. *Atmosphere* **9**, 5 (2018).
35. Zhang, Y. et al. The controlling factors of atmospheric formaldehyde (HCHO) in Amazon as seen from satellite. *Earth Space Sci.* **6**, 959–971 (2019).
36. Sheng, J. et al. Monsoon-driven transport of organochlorine pesticides and polychlorinated biphenyls to the Tibetan Plateau: three year atmospheric monitoring study. *Environ. Sci. Technol.* **47**, 3199–3208 (2013).
37. Alvarado, L. et al. Unexpected long-range transport of glyoxal and formaldehyde observed from the Copernicus Sentinel-5 Precursor satellite during the 2018 Canadian wildfires. *Atmos. Chem. Phys.* **20**, 2057–2072 (2020).
38. Seftor, C. et al. Postlaunch performance of the Suomi National Polar-orbiting partnership Ozone Mapping and Profiler Suite (OMPS) nadir sensors. *J. Geophys. Res. Atmos.* **119**, 4413–4428 (2014).
39. González Abad, G., Vasilkov, A., Seftor, C., Liu, X. & Chance, K. Smithsonian astrophysical observatory ozone mapping and profiler suite (SAO OMPS) formaldehyde retrieval. *Atmos. Meas. Tech.* **9**, 2797–2812 (2016).
40. Landgraf, J. et al. Carbon monoxide total column retrievals from TROPOMI shortwave infrared measurements. *Atmos. Meas. Tech.* **9**, 4955–4975 (2016).
41. Poli, P. et al. ERA-20C: an atmospheric reanalysis of the twentieth century. *J. Clim.* **29**, 4083–4097 (2016).
42. Morisette, J. T. et al. Validation of MODIS active fire detection products derived from two algorithms. *Earth Interact.* **9**, 1–25 (2005).

Acknowledgements

This work is supported by the National Key Research and Development Program of China (2022YFC3700100, 2023YFC3706205), the National Natural Science Foundation of China (42225504, 42305199 and 42205151), the National Natural Science Foundation of China (U21A2027), and the Major Project of High Resolution Earth Observation System (Grant No. "30-Y60B01-9003-22/23").

Author contributions

Conceptualization, W.S., Q.H., and C.L.; Methodology, W.S., Q.H., C.Z., and C.L; Software, Y.X.; Formal Analysis, Y.X.; Investigation, W.S., and Y.X.; Data Curation, Y.X.; Writing-Original Draft, Y.X.; Writing-Review & Editing, Y.X., W.S., Y.T., H.H., and Z.J.; Visualization, Y.X.; Supervision, W.S., and C.L.

Competing interests

The authors declare no competing interests.

Additional information

Supplementary information The online version contains supplementary material available at https://doi.org/10.1038/s41612-024-00639-9.

Correspondence and requests for materials should be addressed to Wenjing Su or Cheng Liu.